U.S. DEPARTMENT OF ENERGY | Office of Science

DOE/SC-ARM-TR-335

BNF Radar b1 Data Processing Report: Spring 2025

M Rocque
M Deng
E Schuman
T Wendler
A Theisen
A Matthews
Y-C Feng
I Lindenmaier
V Castro

April 2026

ARM

DISCLAIMER

BNF Radar b1 Data Processing Report: Spring 2025

M Rocque, Pacific Northwest National Laboratory (PNNL)
A Matthews, PNNL
M Deng, Brookhaven National Laboratory
Y-C Feng, PNNL
E Schuman, PNNL
I Lindenmaier, PNNL
T Wendler, PNNL
V Castro, PNNL
A Theisen, Argonne National Laboratory

April 2026

How to cite this document:

Rocque, M, A Matthews, M Deng, Y-C Feng, E Schuman, I Lindenmaier, T Wendler, V Castro, and A Theisen. 2026. SAIL BNF Radar b1 Data Processing Report: Spring 2025. U.S. Department of Energy, Atmospheric Radiation Measurement User Facility, Richland, Washington. DOE/SC-ARM-TR-335.

Work supported by the U.S. Department of Energy,
Office of Science, Office of Biological and Environmental Research

Acronyms and Abbreviations

2D	two-dimensional
AGL	above ground level
AMF	ARM Mobile Facility
ARM	Atmospheric Radiation Measurement
ARMOR	Advanced Radar for Meteorological and Operational Research
BNF	Bankhead National Forest
CSAPR2	C-band Scanning ARM Precipitation Radar
DQR	Data Quality Report
DSD	drop size distribution
GE	general sensitivity
HSRHI	hemispheric range height indicator
IOP	intensive operational period
KaSACR	Ka-band Scanning ARM Cloud Radar
KAZR2	Ka-band ARM Zenith Radar
LD	laser disdrometer
LDQUANTS	Laser Disdrometer Quantities Value-Added Product
LDR	linear depolarization ratio
MD	moderate sensitivity
MET	surface meteorological instrumentation
NEXRAD	Next-Generation Weather Radar
PLO	phase-locked oscillator
PNNL	Pacific Northwest National Laboratory
PPI	plan position indicator
PR	precipitation sensitivity
RHI	range height indicator
RWP	radar wind profiler
SACR	Scanning ARM Cloud Radar
SONDE	balloon-borne sounding system
TRACER	Tracking Aerosol Convection Interactions Experiment
UAH	University of Alabama – Huntsville
UTC	Coordinated Universal Time
VDIS	video disdrometer
VPT	vertically pointing scan
WRA	wet radome attenuation
XSACR	X-band Scanning ARM Cloud Radar
ZDR	differential reflectivity

Contents

Figures

Tables

1.0 Introduction

The U.S. Department of Energy's Atmospheric Radiation Measurement (ARM) User Facility supports atmospheric science through an integrated network of fixed and mobile observatories. These facilities collect continuous and campaign-based observations of atmospheric properties, with the goal of improving the representation of clouds, aerosols, precipitation, and radiation in Earth system models. The Bankhead National Forest (BNF) site, established as an ARM Mobile Facility (AMF) on 1 October 2024, is situated in a forested region of northern Alabama. Its strategic location in a southeastern U.S. environment characterized by complex terrain, diverse land cover, and frequent convective storms provides a valuable opportunity to examine coupled land-atmosphere processes under natural variability.

The BNF campaign focuses on understanding how forest canopy structure, surface fluxes, and regional meteorology influence the formation and evolution of boundary-layer clouds and precipitation systems. In support of this goal, a suite of remote-sensing, in situ, and profiling instruments have been deployed. Among these are a vertically pointing Ka-band radar and three scanning radars at Ka-, X-, and C-band. This report details the operations of these radars during the spring of 2025 and the methods for generating high-quality b1-level data.

1.1 Overview of BNF Radars

A cornerstone of the BNF observatory is the second-generation Ka-band ARM Zenith Radar (KAZR2; Figure 1), a cloud-profiling radar operating at 35 GHz (Table 1). The KAZR2 is designed for high-sensitivity observations of hydrometeors in the vertical column. The KAZR2 has three modes of operation that are optimized for different meteorological conditions:

- General sensitivity (GE) mode: Short-pulse transmission for high temporal and spatial resolution in the lowest 1-2 km AGL. Ideal for shallow clouds and near-surface returns.
- Moderate sensitivity (MD) mode: Frequency-modulated continuous wave or chirped-pulse transmission for improved sensitivity at higher altitudes, at the cost of a near-radar blind zone.
- Precipitation sensitivity (PR) mode: Short-pulse, lower-gain mode for sampling moderate-to-heavy rainfall rates without saturation.

The KAZR2 at BNF is located at the main facility within the heart of the forest (Figure 2).

In addition to the KAZR2, ARM also operates the dual-frequency Scanning ARM Cloud Radar (SACR) at Ka- and X-band frequencies. These two radars share the same pedestal and thus perform the same scan types (Figure 1). The KaSACR transmits a single channel while the XSACR is dual-polarized. While the gate spacing for both radars is 25 m, the XSACR maximum range is about 2.5 times that of KaSACR (Table 1). The SACR is located at the S4 supplementary site about 16.5 km northeast of the main site on the other side of a terrain ridge (Figure 2, Table 2).

The final radar is the second-generation C-band Scanning ARM Precipitation Radar (CSAPR2; Figure 1), which is a dual-polarized weather radar operating with a range of 110 km (Table 1). In addition to typical radar moments including reflectivity, mean Doppler velocity, and spectral width, the CSAPR2 measures

differential reflectivity (ZDR), correlation coefficient (ρ_{hv}), and differential phase. The dual-polarization nature of the radar and the C-band operating frequency allow for more in-depth analysis of stronger convective systems that the cloud radars may not provide. The CSAPR2 is located at the S3 supplementary site about 21 km northeast of the SACR site (37 km from the main site; Figure 2, Table 2).

Table 1. BNF radar specifications.

Radar	Frequency (GHz)	Polarization	Gate spacing (m)	Maximum range (km)	Nyquist velocity (m s^{-1})
KAZR2	34.8	transmit single receive dual	30	16.7	8.5
KaSACR	35.3	transmit single receive dual	25	18.9	11.1
XSACR	9.7	dual	25	46.6	17.8
CSAPR2	5.7	dual	100	110	16.5

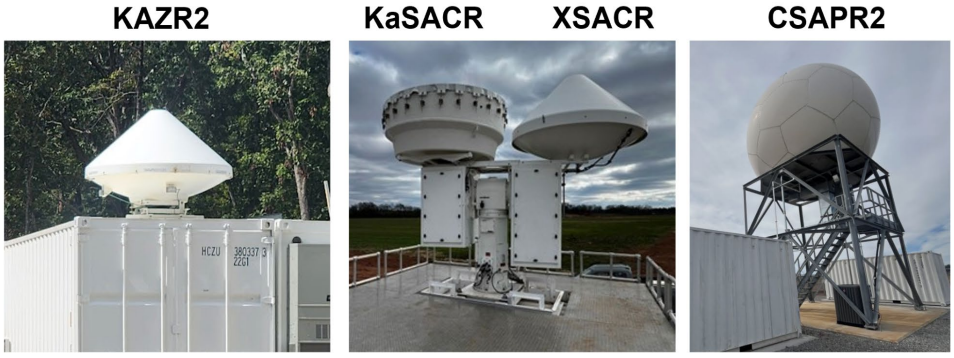

Figure 1. ARM radars installed at BNF from left to right: KAZR2 (M1 site), KaSACR and XSACR (S4 site), and CSAPR2 (S3 site).

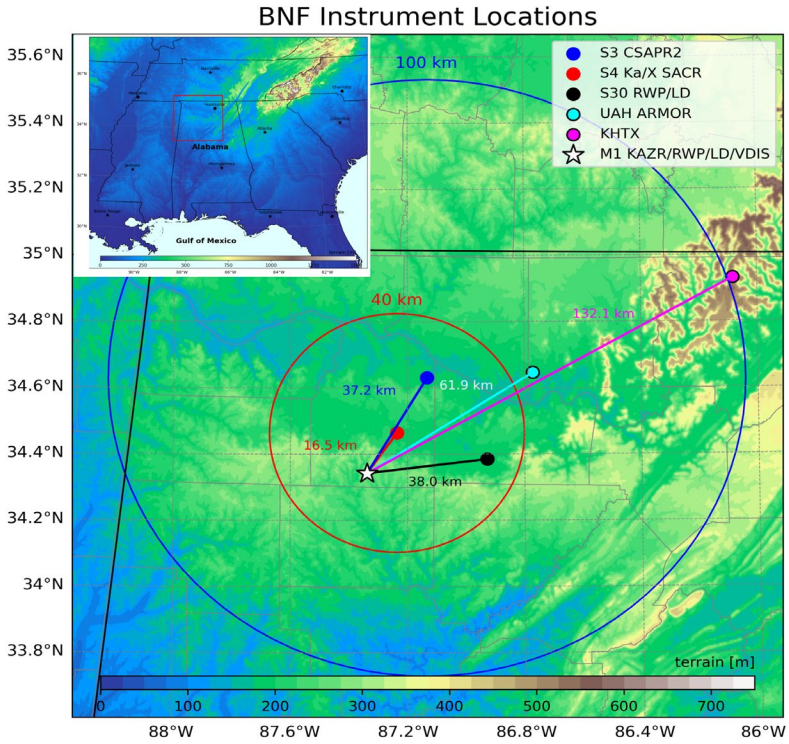

Figure 2. Location of ARM radar sites (KAZR2: white star, SACR: red dot, CSAPR2: blue dot) deployed for BNF. The XSACR 40-km range ring is shown in red and the CSAPR2 100-km range ring is shown in blue. Additional sites depicted include the ARM S30 site (black dot), the University of Alabama – Huntsville (UAH) Advanced Radar for Meteorological and Operational Research (ARMOR; cyan dot) and the Huntsville/Hytop WSR-88D (KHTX; magenta dot). Terrain heights (m) are shaded and the insert depicts the southeast U.S. for context.

Table 2. Location of ARM radar sites relative to one another and the Next-Generation Weather Radar (NEXRAD) KHTX.

Site/Radar	Relevant instruments	Latitude/ longitude	Distance to KAZR (km)	Distance to SACR (km)	Distance to CSAPR2 (km)
M1	KAZR, LD, VDIS, RWP, MET, SONDE	34.3425 -87.3382	–	16.47	37.16
S3	CSAPR2	34.6308 -87.1331	37.16	20.77	–
S4	Ka/X SACR	34.4643 -87.2360	16.47	–	20.77
S30	RWP, LD, MET	34.3848 -86.9279	37.95	29.61	33.19
KHTX	WSR-88D	34.9306 -86.0833	132.10	117.42	101.48

1.2 Scan Strategy

From April through June 2025, the BNF radars were performing consistent scans initially designed by the principle investigator team for the radar intensive operational period (IOP). The SACR performed eight plan position indicators (PPIs) that varied in elevation from 1.5° to 17.0° (Figure 3a, Table 3). The six-minute heartbeat then concluded with two hemispheric range height indicators (HSRHIs) over the KAZR2 site. The CSAPR2 performed 15 PPIs covering the same initial elevation angles as SACR but with several additional ones to increase the coverage near the surface and aloft (Figure 3b, Table 3). The roughly 10-minute heartbeat concluded with one RHI over the KAZR2 site starting at 90° to estimate the ZDR offset.

Table 3. Scan strategy for BNF radars during the April-June 2025 IOP.

Radar	Scan type	Azimuths (deg)	Elevations (deg)	Range (km)
KAZR2	VPT	N/A	90.0	16.7
KaSACR/XSACR	8 PPIs	0-360	1.5, 2.5, 3.5, 4.5, 7.0, 10.0, 13.0, 17.0	18.9 (Ka) 46.7 (X)
	2 HSRHI	214	0-180	18.9 (Ka) 46.7 (X)
CSAPR2	15 PPIs	0-360	1.5, 2.5, 3.5, 4.5, 5.5, 6.5, 8.0, 10.0, 12.0, 14.0, 17.5, 21.5, 26.0, 33.0, 42.0	110
	RHI	90-1.5	210	110

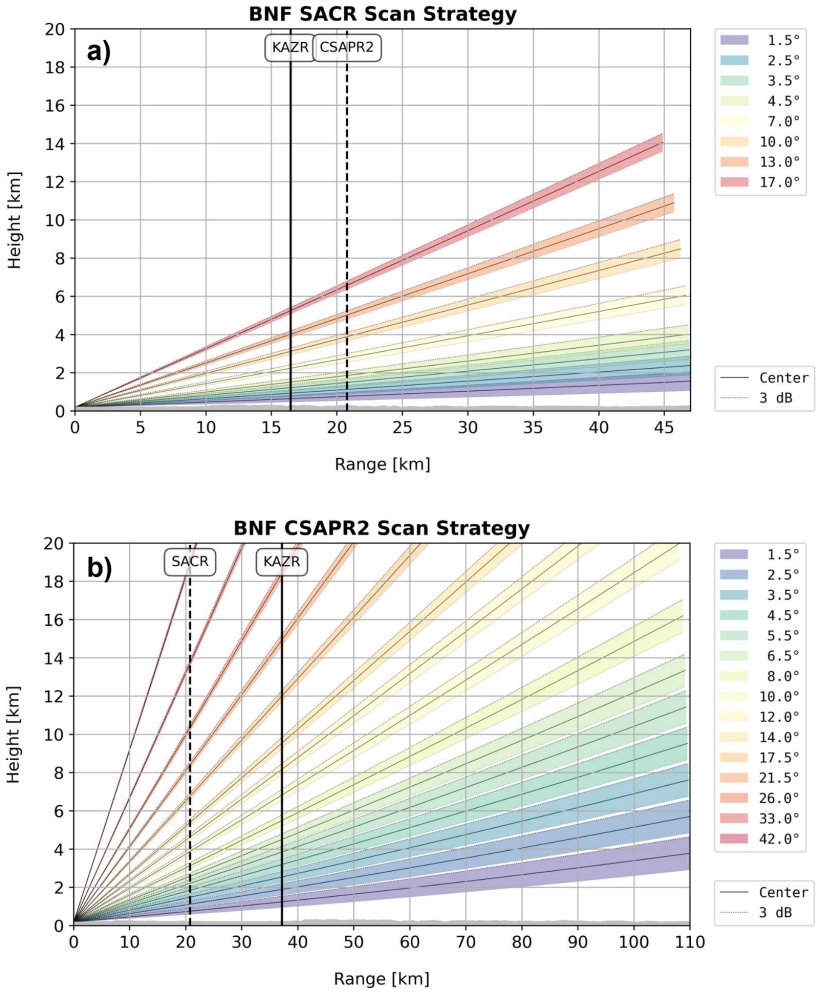

Figure 3. a) BNF SACR PPI elevation angles shown as a function of range (km) and height (km). The KAZR2 and CSAPR2 distances are included as vertical solid and dashed black lines, respectively. b) As in a) but for the BNF CSAPR2 PPIs. The KAZR2 and SACR distances are included as vertical solid and dashed lines, respectively.

1.3 Radar Performance

The KAZR2 was the first radar to become operational at BNF, with data collection starting in mid-November 2024. The data availability for the KAZR2 is shown in Figure 4a for November 2024 through June 2025. KAZR2 operations were quite consistent with a few notable data gaps in February due to issues with the air conditioning system.

Meanwhile for the scanning radars, the SACR began collecting data in December 2024 while the CSAPR2 became operational in mid-February 2025. These radars were considered to be in a testing period until 1 April 2025 when the radar IOP began. Data availability during the IOP for the scanning radars is shown in Figure 4. A significant gap in SACR data is visible in mid-June (13-26 June), which can be attributed to a broken fiber optic cable. The CSAPR2 stopped operating on 23 June due to a

serious mechanical problem with the pedestal. Total data availability during the IOP for the SACR and CSAPR2 was 81% and 84%, respectively.

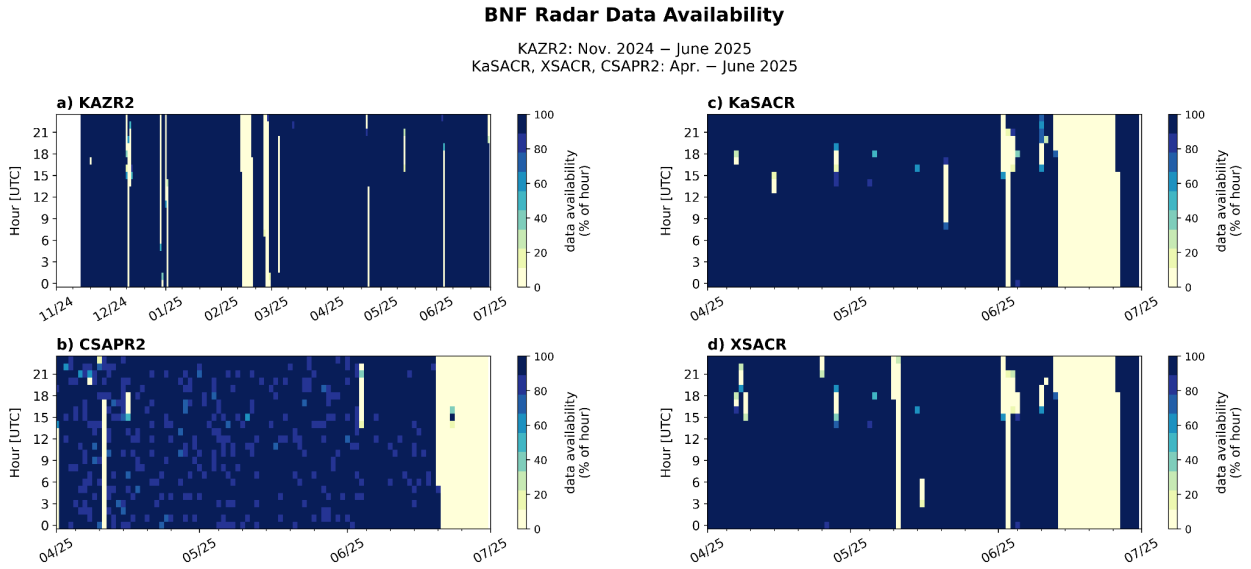

Figure 4. BNF radar data availability for a) KAZR2 from November 2024 through June 2025. Colors indicate the percentage of data available per hour. b) As in a) but for CSAPR2 for April through June 2025. c-d) as in b) but for KaSACR and XSACR.

1.4 Overview of b1 Processing

The b1 processing methods applied to the BNF radars and the subsequent results are detailed below for the spring of 2025. The processing methods are similar to those applied for past ARM field campaigns, especially the Tracking Aerosol Convection Interactions Experiment (TRACER; Feng et al. 2024). For the KAZR2, reflectivity offsets are estimated for each mode and non-meteorological echo classification masks are developed to filter out insects and other clutter. For the KaSACR, reflectivity offsets are estimated and a basic censor mask is developed that distinguishes signal from background noise. For the XSACR and CSAPR2, reflectivity and ZDR offsets are estimated, specific differential phase (KDP) is derived, attenuation due to hydrometeors is estimated for reflectivity and ZDR, and basic censor masks are developed.

2.0 KAZR2

2.1 Reflectivity Offsets for GE Mode with Disdrometer Measurement

The wet radome attenuation (WRA) calibration technique, recently developed by Deng et al. (2024), accounts for the two-way attenuation caused by a film of water accumulating on the radar radome during rainfall events. At Ka-band frequencies, this attenuation is significantly more pronounced than at lower-frequency radars, due to the stronger interaction between microwave radiation and water layers on the radome surface. WRA can bias measured reflectivity by up to several decibels during rain.

The WRA technique involves comparing radar-measured reflectivity (Ze) from GE mode with disdrometer-derived Ze values, computed from drop size distributions (DSDs) measured at the surface. The difference in reflectivity, $\Delta Ze = Ze\_disdrometer - Ze\_radar$, is expected to increase linearly with rain rate in logarithmic space. A log-linear regression is performed, with the slope representing WRA sensitivity and the intercept representing a constant radar calibration bias. In the evaluation of this calibration method with other methods during TRACER (Deng et al. 2024), this method yields calibration uncertainty on the order of ±3 dB.

Figure 5 shows the Ze offset time series against the disdrometer Ze values for the GE mode at BNF during rainy days. The fitted log-linear slope depends on the radar radome type and age, and hence the expected WRA dependence. Given the conical shape of the KAZR2 radome (Figure 1), the slope for log-linear fitting is 6 for BNF. This slope is lower than the one used during the TRACER campaign (8) with a KAZR that had a flatter radome. The intercept provides the estimated calibration offset needed to align the radar with the disdrometer reference. The estimated Ze offset for the GE mode can be split into two time periods, one before 15 December 2024 when the offset was near 0 dB and one after when the offset increased to around 4 dB (KAZR2 biased high). As mentioned earlier, work was performed on the KAZR2 transmitter to increase the output power in mid-December. The Ze offset tracks with changes in the transmit power and radar calibration constant (not shown).

2.2 Reflectivity Offsets for MD and PR Mode through Intermode Comparison

Relative reflectivity offsets for MD and PR modes are calculated through intermode comparison for GE versus PR and GE versus MD. Time series of these differences where the signal-to-noise ratio (SNR) is greater than 0 dB are shown in Figure 5. In November and December 2024, the offsets are consistent at around -0.3 dB for the PR comparison and -0.8 dB for the MD comparison. In mid-December, work was performed on the transmitter to increase the output power. This resulted in a reflectivity shift between the modes and a steady increase in the difference over time. The GE versus PR difference is more substantial, with a starting value of around 1.3 dB on 15 December 2024 and a slope of 2.3 dB $year^{-1}$. The GE versus MD difference is not as significant, starting around 0.2 dB on 15 December 2024 with a slope of 0.7 dB $year^{-1}$. The slopes of the differences are related to drifts in the transmit power that impact the radar calibration constants (not shown).

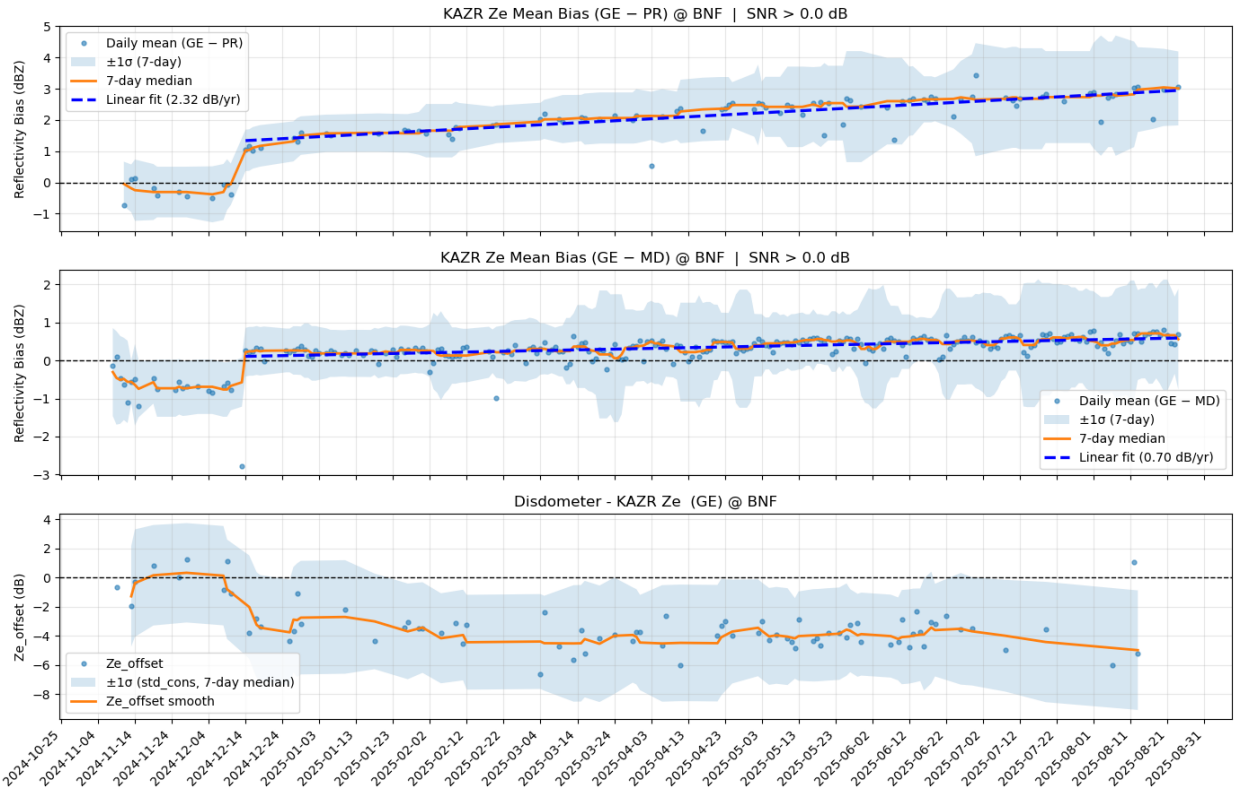

Figure 5. (top) Time series of BNF KAZR2 daily mean GE-PR reflectivity offsets (blue dots), with the weekly running median shown as the orange line and the standard deviation above and below the median shown as the shaded blue region. A linear fit is applied to the data starting 15 December 2024 with a slope of 2.3 dB year^{-1}. (middle) As in (top) but for GE-MD reflectivity offsets. The linear fit has a slope of 0.7 dB year^{-1}. (bottom) Time series of Ze offset for the KAZR2 GE mode estimated from the WRA calibration technique.

2.3 Non-Meteorological Echo Mask

Two masks are included in the b-level data for the KAZR2: a censor mask and a classification mask. The censor mask uses velocity texture to distinguish between signals and background noise. Examples of the censor mask for each mode are shown in Figure 6 for 28 March 2025. The classification mask identifies additional non-meteorological signals that are not otherwise filtered out with the censor mask. The classification mask categories are background noise, ground clutter, range sidelobes (only for the MD mode), and biota (most likely insects). Pixels that are not classified in one of these four categories are considered to be hydrometeors. Examples of the classification mask are also shown in Figure 6. Insects are frequently observed by the KAZR2 and have similar radar characteristics as those at the Southern Great Plains site. The linear depolarization ratio (LDR) is the most important field in distinguishing insects from clouds. While the mask is not perfect, it can provide a first pass at removing any unwanted signals.

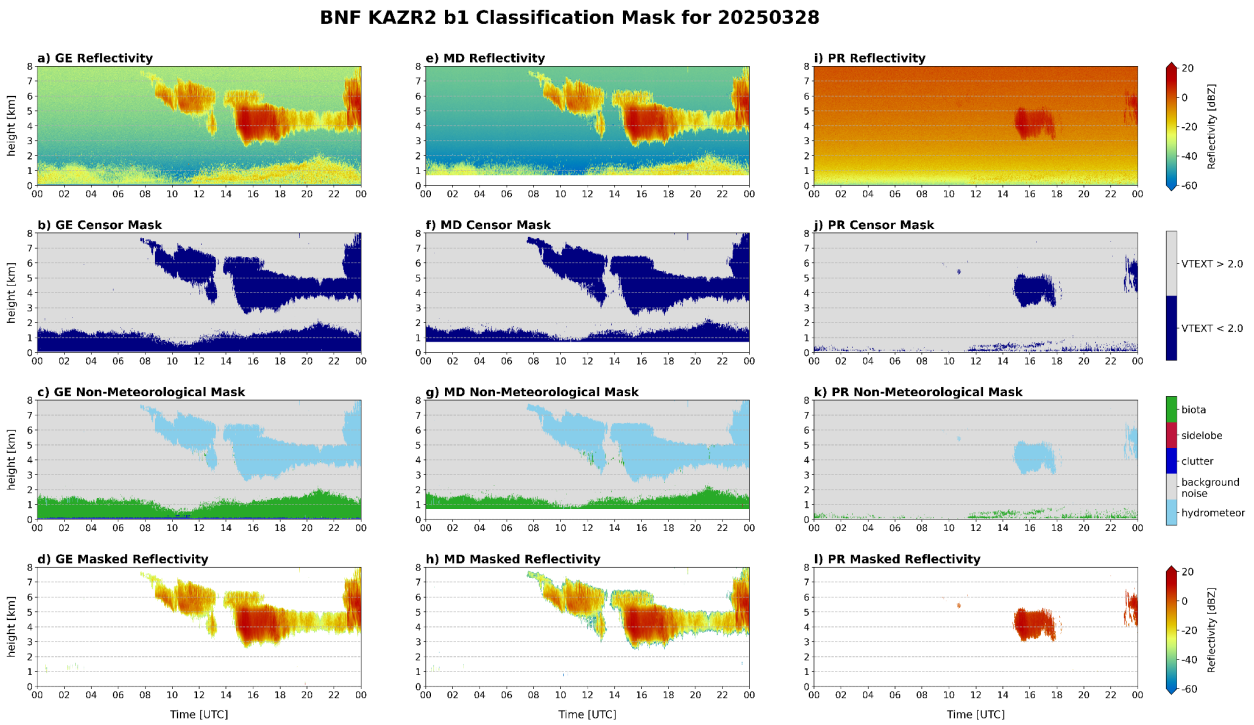

Figure 6. Time-height plots of a-d) BNF KAZR2 GE mode a) reflectivity (dBZ), b) censor mask (velocity texture > 2.0 m s^{-1} = light grey; < 2.0 m s^{-1} = navy blue), c) classification mask (hydrometeor = light blue; background noise = light grey; clutter = blue; sidelobe = red; biota = green), and d) masked reflectivity (dBZ) on 28 March 2025. e-h) as in a-d) but for the MD mode. i-l) as in a-d) but for the PR mode.

3.0 CSAPR2

3.1 KDP and Attenuation

Specific differential phase (KDP) is the change in differential phase along a radial and is a derived quantity that can be related to the amount of liquid water in the atmosphere, making it particularly useful for estimating rain attenuation. Specific attenuation (A_h; dB km^{-1}), specific differential attenuation (A_{DP}; dB km^{-1}), and KDP (° km^{-1}) are calculated in the Laser Disdrometer Quantities Value-Added Product (LDQUANTS; Hardin et al. 2020) and relationships between the quantities can be derived and applied to the radar measurements. At BNF, A_h-KDP and A_{DP}-KDP equations from LDQUANTS at the main site are derived for C-band and X-band frequencies and shown in Figure 7. Note that X-band has much higher coefficients compared to C-band. These relationships were also derived using data from the laser disdrometer at the S30 supplementary site and the video disdrometer at the main site and the coefficients were very similar. Once the appropriate relationships have been determined, KDP from the radar is then estimated using the CSU RadarTools python package (Lang et al. 2024) `calc_kdp_bringi` module (Hubbert and Bringi 1995). Examples of the KDP estimation for two cases are shown in Figure 7. There are clear gradients in the differential phase that correspond to regions of higher reflectivity and positive KDP values. Coefficients from the A_h-KDP and A_{DP}-KDP relationships derived from the disdrometer for C-band (Figure 7) are then used with the calculated KDP to estimate

rain attenuation and differential attenuation. Examples of the specific attenuation and the reflectivity with the attenuation applied are also included in Figure 8.

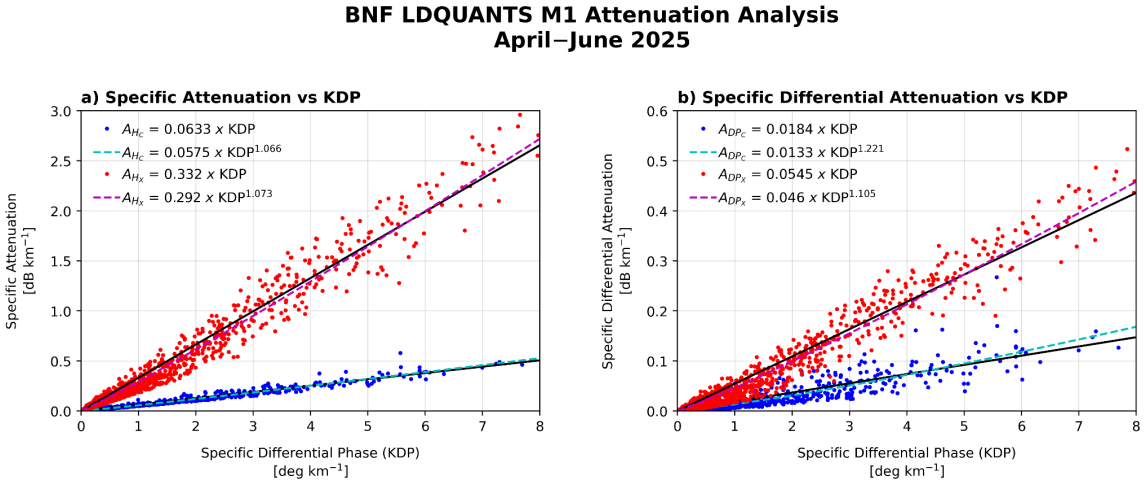

Figure 7. a) Specific attenuation (dB km^{-1}) versus specific differential phase (KDP; ° km^{-1}) measured from the laser disdrometer value-added product (LDQUANTS) at the main site for C-band (blue) and X-band (red). b) As in a) but specific differential attenuation (dB km^{-1}).

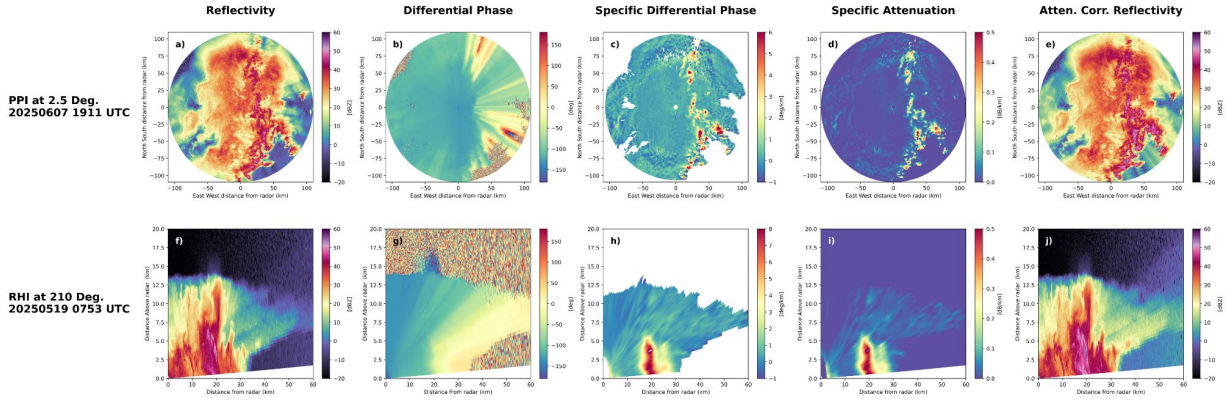

Figure 8. a-e) CSAPR2 PPIs at 2.5° elevation at 1911 UTC on 7 June 2025 and f-j) CSAPR2 RHIs at 210° azimuth at 0753 UTC on 19 May 2025.

3.2 Reflectivity Offsets

The stability of the radar is first evaluated by monitoring the reflectivity of ground clutter targets over time. Figure 9 shows the reflectivity and mean Doppler velocity of targets within 10 km of the radar and the points that are determined to be clutter where reflectivity is greater than 40 dBZ and the absolute mean Doppler velocity is less than 0.1 m s^{-1}. The daily average 95th percentile of the reflectivity values from these points are then plotted as a function of time (Figure 9d). There is a slight decline in the reflectivity through May 2025 and then an increase in early June that can be attributed to a calibration routine performed by the engineers. The rate of decline is about 0.5 dB per month.

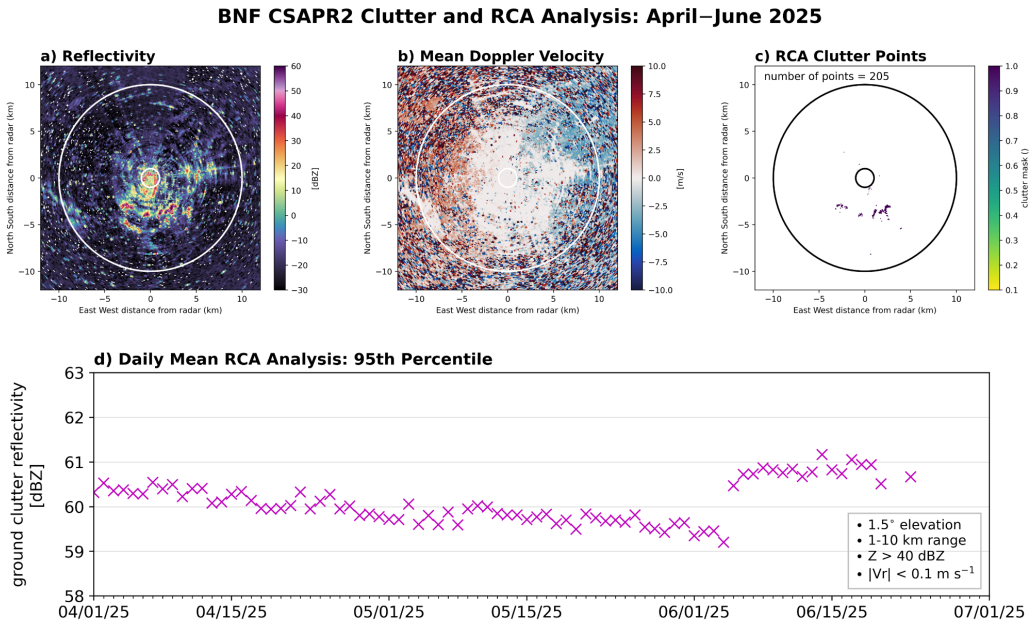

Figure 9. a-c) PPIs of a) reflectivity (dBZ), b) mean Doppler velocity (m s^{-1}), and c) clutter points identified for stability monitoring from the CSAPR2. PPIs are zoomed in to the nearest 12 km and the 10-km range ring is shown in each plot. d) Time series of daily mean 95th percentile ground clutter reflectivity from April through June 2025.

To evaluate the CSAPR2 systematic reflectivity offset, reflectivity values are compared with the nearest WSR-88D (KHTX; Huntsville/Hytop, Alabama) located about 100 km northeast of the S3 site. Data are matched in space and time (within 500 m and 1 minute) and comparison points are extracted where the ρ_{HV} of both radars is greater than 0.95. The CSAPR2 measurements are corrected for rain attenuation using the A_h-KDP relationship derived in Figure 7. The mean offset between CSAPR2 and KHTX calculated when points are between 10 and 40 dBZ was -1.9 dB for the IOP (Figure 10). This offset is fairly consistent over time (Figure 11), with the average of the daily mean reflectivity offsets around -1.7 dB. This comparison was also performed with KGWX (Columbus Air Force Base, Mississippi), which is farther than KHTX, and the results were within 1 dB, suggesting the CSAPR2 has a reflectivity offset of about 2.0 dB. This value also matches well with the previously discussed ARM radar comparisons, further highlighting the robustness of this method.

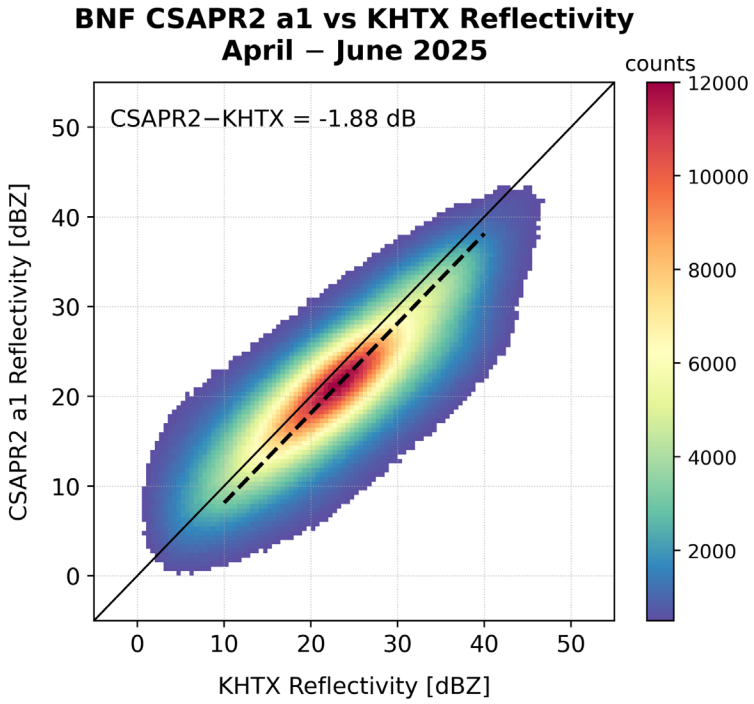

Figure 10. 2D histogram of BNF CSAPR2 a1 reflectivity versus KHTX reflectivity with colors corresponding to the number of points within each bin. A one-to-one line is shown in solid black, and a fitted line for reflectivity between 10 and 40 dBZ is shown in the dashed black line. The mean offset between CSAPR2 and KHTX is -1.9 dB.

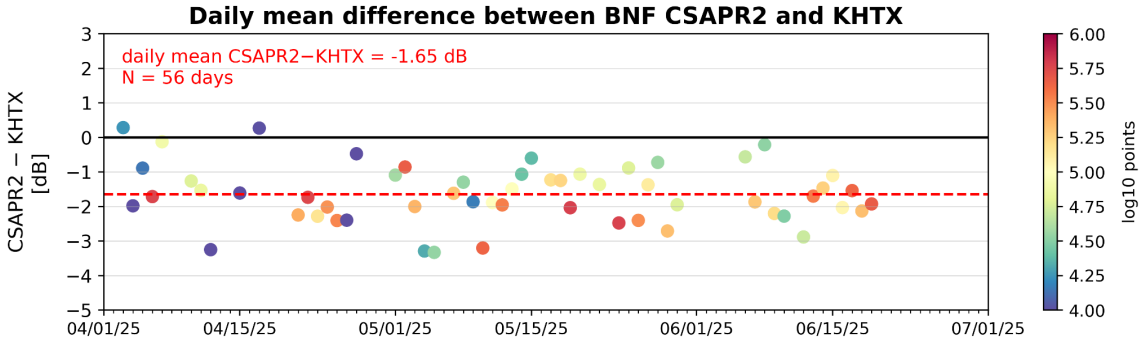

Figure 11. Time series of the daily mean differences between BNF CSAPR2 a1 and KHTX reflectivity (dB) for April through June 2025. Each point is colored by the number of good comparison gates for that day. The mean of the daily mean differences is shown in the upper left (-1.7 dB), and is plotted as the red dashed line. 56 days of data were used.

3.3 Differential Reflectivity Offsets

Given the scan strategy of the CSAPR2, ZDR offsets were estimated using data from the RHIs near vertical. Before the IOP, several test scans were performed to determine if the RHI method would be suitable for ZDR offset estimation compared to true vertically pointing scans (VPTs). Figure 12 shows the estimated ZDR offset from VPTs and the estimated ZDR offset from RHIs using elevations between 85° and 90° during the test period at the end of March. Comparison points are limited between 600 m and

2 km and are only selected during light precipitation times (reflectivity < 25 dBZ, SNR > 10 dB, and ρ_{hv} > 0.95). While there is more variability using the RHI method, the average offset is the same between methods. The RHI method was applied for the entire IOP and the estimated ZDR offset was found to be consistent over time at around -0.8 dB (Figure 13).

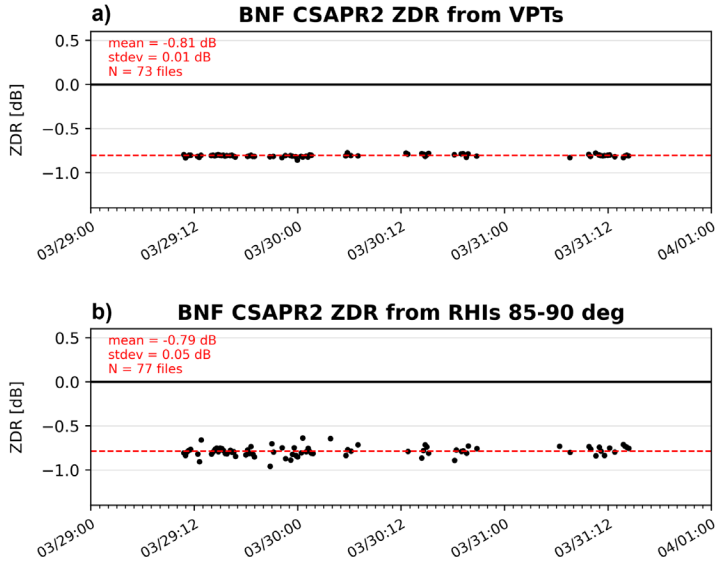

Figure 12. Time series of ZDR offsets (dB) from the BNF CSAPR2 estimated using a) vertically pointing scans (VPTs) and b) RHIs between 85-90° elevation for 29-31 March 2025.

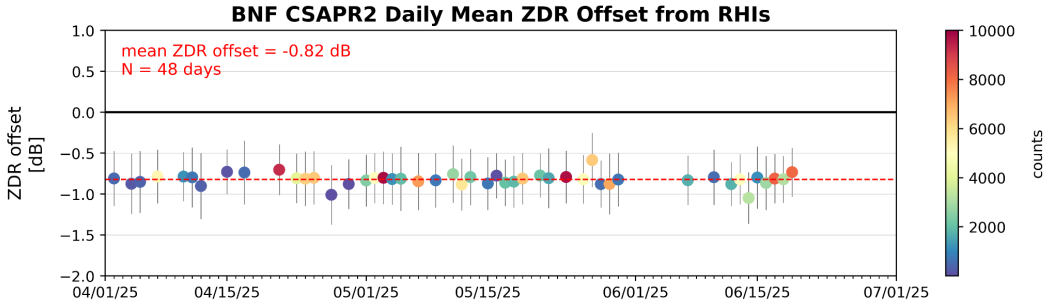

Figure 13. Time series of the daily mean ZDR offset (dB) estimated from the CSAPR2 RHIs. Each point is colored by the number of good points, and the error bars represent the standard deviation for that day. The mean of the daily mean differences is shown in the upper left (-0.8 dB), and is plotted as the red dashed line. 48 days of data were used from 1 April to 1 July 2025.

3.4 Classification Mask

The CSAPR2 has a built-in classification from the vendor that identifies various non-meteorological echoes including second- and third-trip echoes, interference, clutter, and sunspokes. An example of the classification mask is shown in Figure 14. ρ_{hv} can also be used to filter out non-meteorological signals as lower values indicate noise. A ρ_{hv} threshold of 0.7 combined with the classification mask can be applied to isolate weather signals.

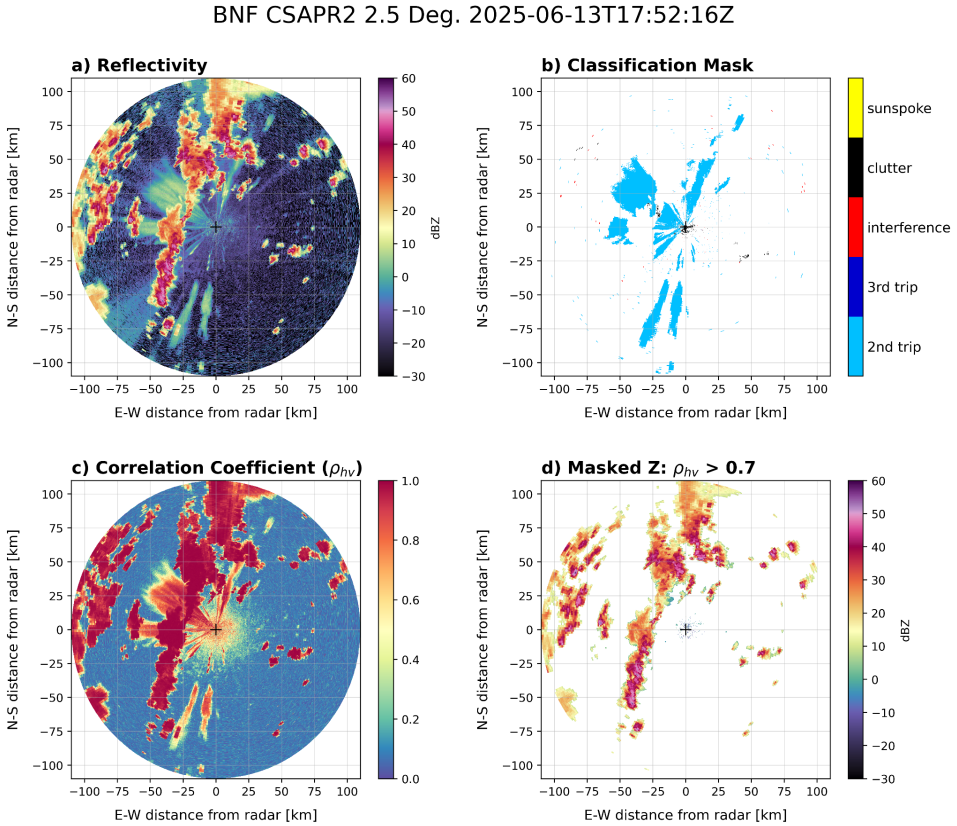

Figure 14. CSAPR2 PPIs at 2.5° elevation of a) reflectivity (dBZ), b) classification mask, c) ρ_{hv}, and d) masked reflectivity (dBZ) at 1752 UTC on 13 June 2025.

3.5 Additional Data Quality Notes

3.5.1 Beam Blockage

The CSAPR2 experiences beam blockage at the lowest elevation angle in the IOP scan strategy (1.5°, Figure 15). The blockage is most prominent to the North, roughly between 345° and 15°, and is likely due to trees surrounding the radar since beam-blockage estimates based on the terrain do not indicate blockage in that direction at that elevation. It is important to note that there are no partial beam-blockage corrections applied for the b-level data.

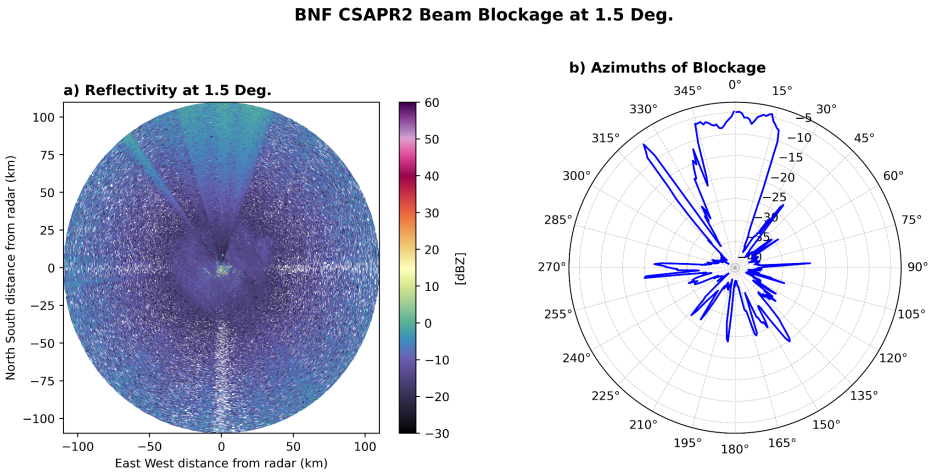

Figure 15. a) BNF CSAPR2 PPI of reflectivity (dBZ) at 1.5° elevation on a clear day and b) average reflectivity between 60 and 100 km across 10 clear days highlighting the azimuth angles where beam blockage is maximized.

3.5.2 Azimuth Flips

Sometimes when the radar failed to complete a PPI sweep, the azimuth angles for the subsequent scans in the heartbeat were shifted 180 degrees. An example of this shift for a case in February is seen in Figure 16 showing ground clutter from normal scans versus ground clutter from scans that are flipped upside down. The azimuth shifts did not occur every time the radar failed to complete a sweep, making it difficult to track. The shifts were likely related to issues with the azimuth encoder and serious mechanical issues with the pedestal. A list of all impacted files is included in the associated ARM Data Quality Report (DQR) D250516.4 and can also be made available upon request. Given the seemingly random nature of this issue, the azimuth flips were not corrected in the b-level data.

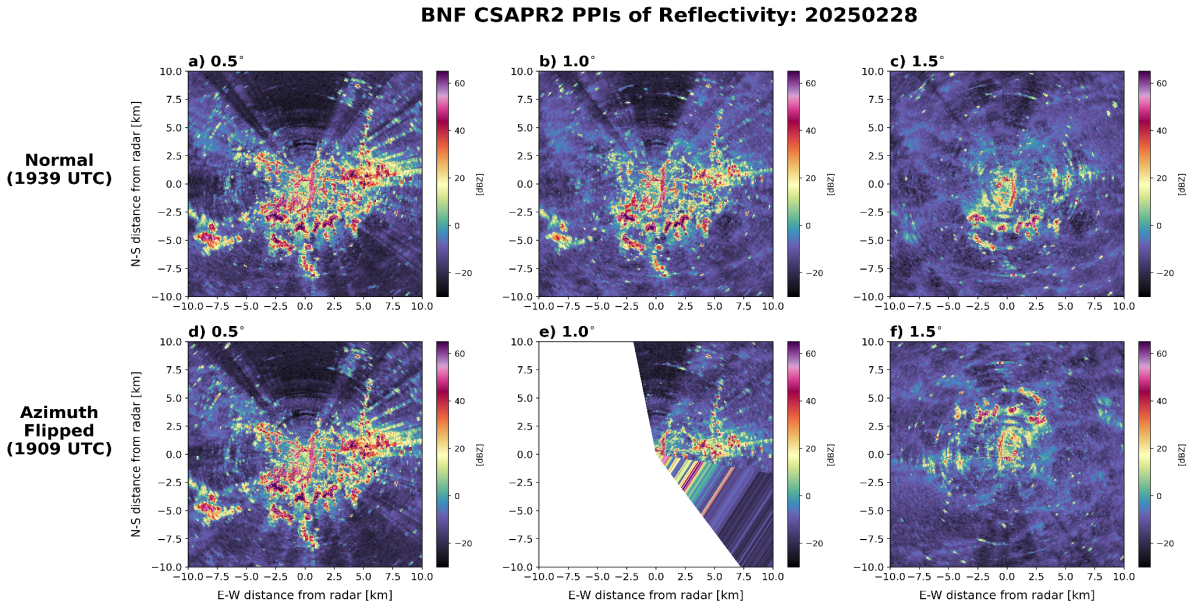

Figure 16. CSAPR2 PPIs of reflectivity zoomed in to the nearest 10 km at a) 0.5° elevation, b) 1.0° elevation, and c) 1.5° elevation at 1939 UTC on 28 February 2025. d-f) as in a-c) but at 1909 UTC when the second sweep fails to complete (e) and the third-sweep azimuths are shifted 180° (f).

4.0 XSACR

4.1 KDP and Attenuation

As with the CSAPR2, KDP is used to estimate the rain attenuation for the XSACR. Two examples of KDP estimation using the CSU RadarTools `calc_kdp_bringi` module (Lang et al. 2024, Hubbert and Bringi 1995) and the subsequent rain attenuation correction applied to the XSACR are shown in Figure 17.

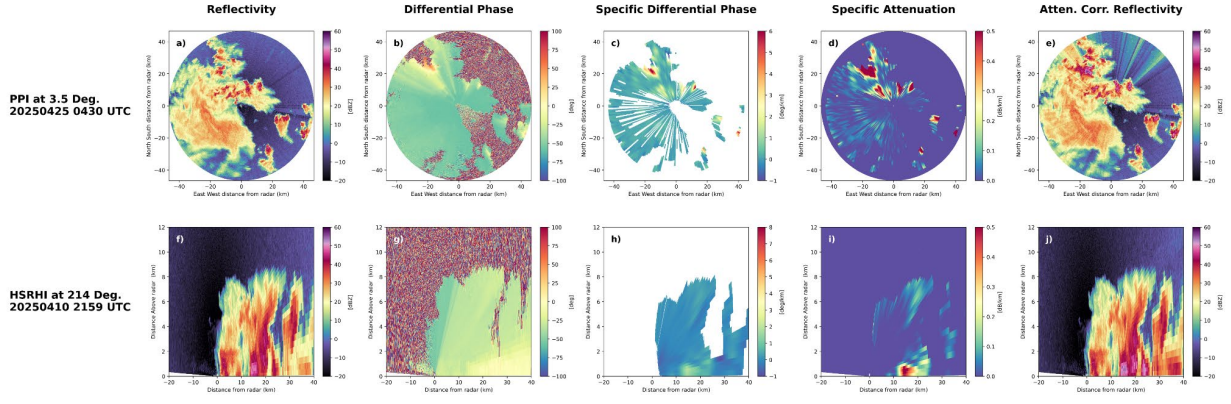

Figure 17. a-e) XSACR PPIs at 3.5° elevation at 0430 UTC on 25 April 2025 of a) reflectivity (dBZ), b) differential phase (°), c) KDP (° km^{-1}), d) specific attenuation (dB km^{-1}), and e) attenuation corrected reflectivity (dBZ). f-j) As in a-e) but of XSACR HSRHIs at 214° azimuth at 2159 UTC on 10 April 2025.

4.2 Reflectivity Offsets

First, to evaluate the stability of the radar we monitored the reflectivity of ground targets over time. Figure 18 shows the reflectivity for the KA (a) and X (b) of the clutter points on a clear day from the lowest PPI elevation (1.5°). The daily average reflectivity of the clutter points is plotted as a function of time (Figure 18c). The XSACR showed a slight decrease throughout this time period, and this was being monitored by the engineering team.

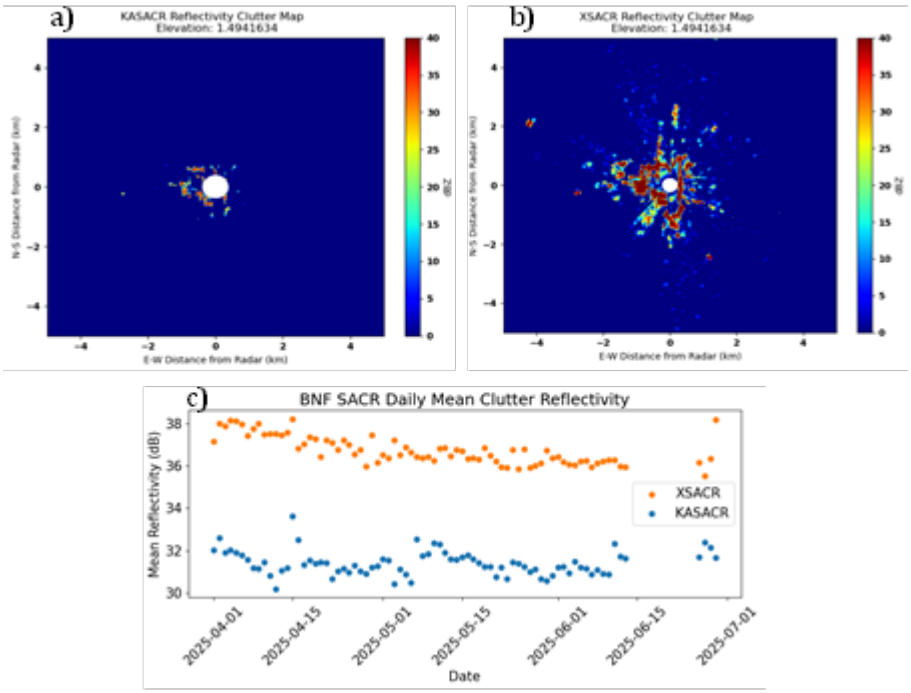

Figure 18. a) Reflectivity of KaSACR clutter, b) reflectivity of XSACR clutter, and c) mean daily reflectivity for the clutter points from each radar.

Next, the XSACR systematic reflectivity offset was evaluated using comparisons with the corrected CSAPR2 system located approximately 20 km to the northeast. Data are matched in space and time (500m and 1 minute) and filtered for data where both radars have a ρ_{HV} greater than 0.95. Then, the mean offset is calculated when reflectivities are between 10 and 40 dBZ. Across all cases of the campaign, the mean difference between these radars was 5.42 dB, as shown in Figure 19. The offset was also fairly consistent in time (Figure 20), with the average being around 5.55 dB. For this data, an XSACR reflectivity offset of +5.5 dB was applied.

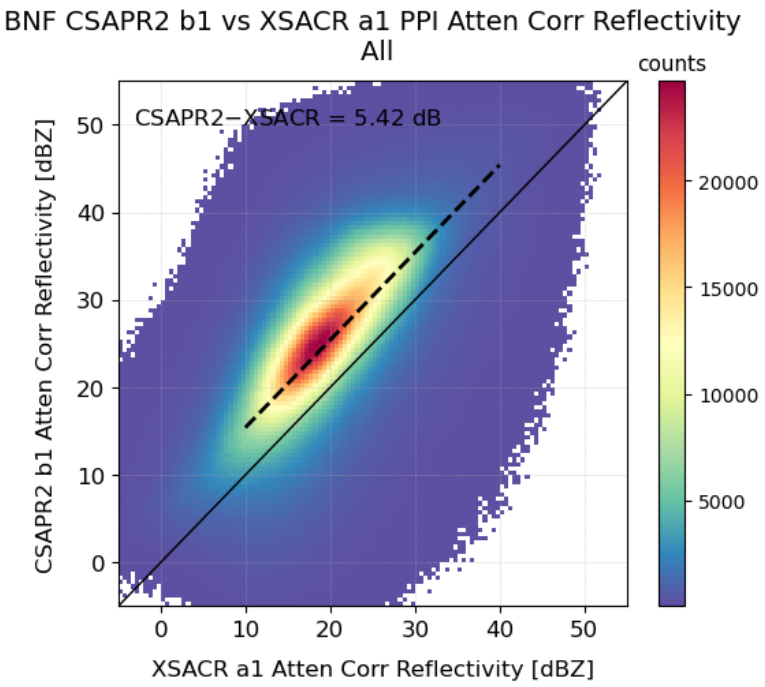

Figure 19. 2D histogram of BNF CSAPR2 versus XSACR reflectivity. Colors correspond to the number of points in each bin. The one-to-one line is shown in solid black, and a fitted line for reflectivity between 10 and 40 dBZ is shown by the dashed black line.

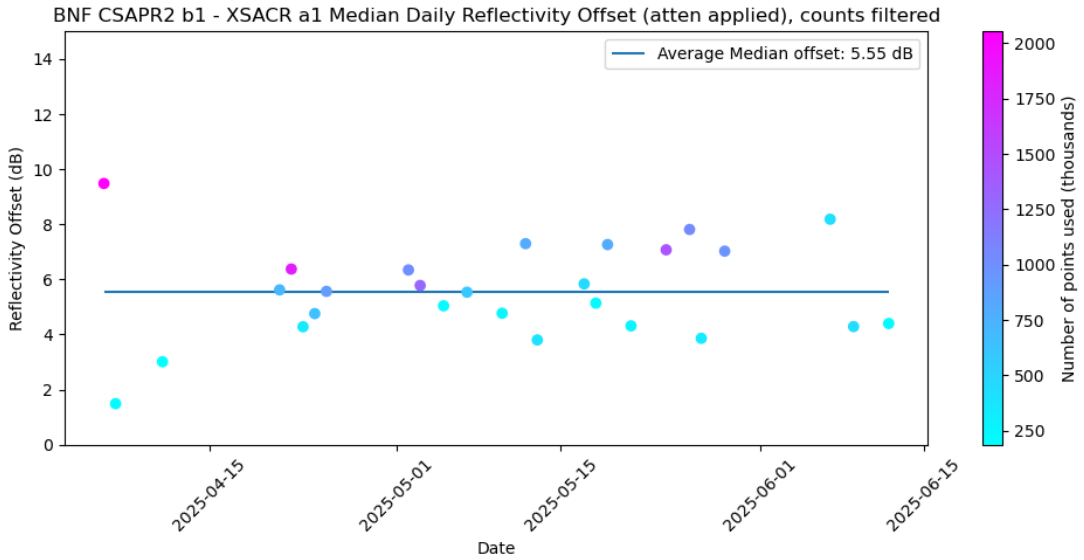

Figure 20. Time series of the daily median reflectivity differences between the CSAPR2 and XSACR. The color corresponds to the number of points passing thresholds, while the solid blue line shows the average median offset.

4.3 Differential Reflectivity Offsets

Typically, ZDR offsets are estimated using vertically pointing scans in light rain. However, because the XSACR scan strategy did not include these scans, data from the HSRHIs within 1 degree of vertical were used to determine the offset. Figure 21 shows the estimated ZDR offset for the near vertical data where reflectivity is less than 30 dBZ, SNR is greater than 0 dB, and ρ_{hv} is greater than 0.985. Over this period, the offset was consistent over time and quite small, at just -0.09. Because the offset is so small and fell within expected uncertainty, a ZDR offset was not applied to the XSACR b1 data.

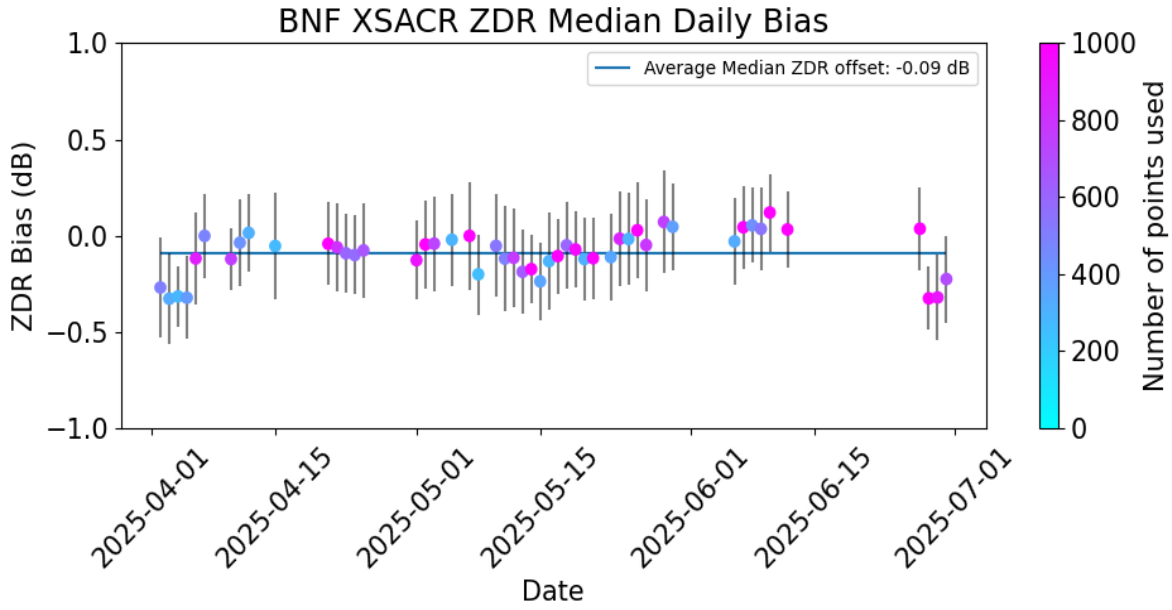

Figure 21. Time series of the daily median ZDR offset in dB from the XSACR HSRHIs. The color corresponds to the number of points passing thresholds and the error bars represent the standard deviation for that day. The average median offset is shown as the blue line.

4.4 Censor Mask

The XSACR does not include a built-in classification mask, so a simple censor mask is created to separate non-meteorological echoes, shown in Figure 22. The filters used for this mask are an SNR threshold of 0 dB and ρ_{hv} of 0.985, and data are stored as a bit mask.

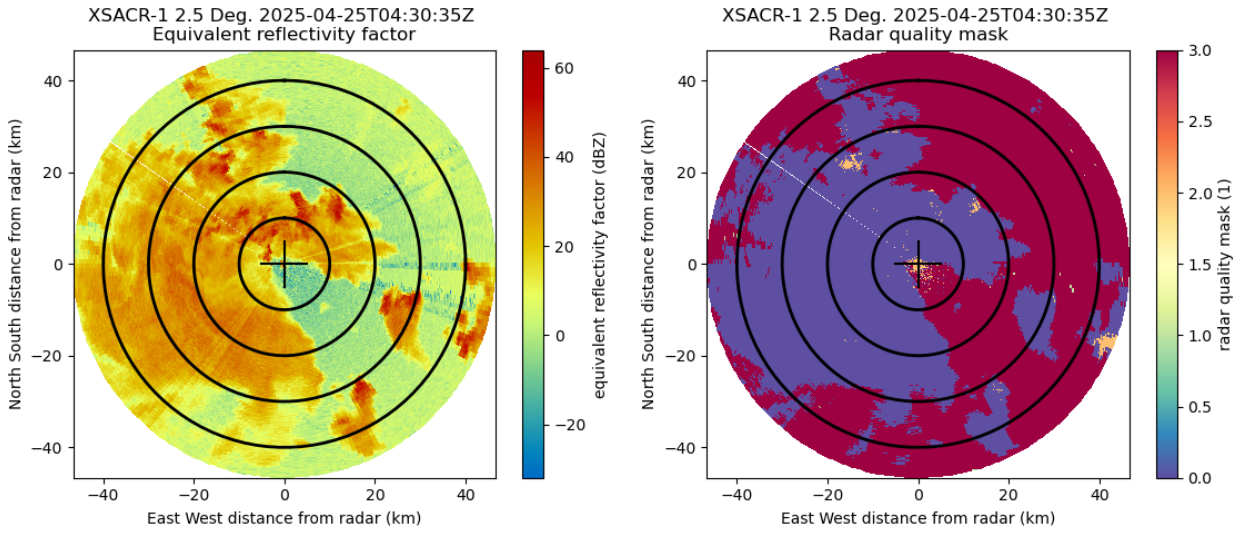

Figure 22. XSACR PPI showing reflectivity (left) and censor mask (right) for a case on 25 April 2025.

4.5 Additional Data Quality Notes

4.5.1 Beam Blockage

The XSACR experiences some beam blockage at the lowest elevation angle (1.5 degrees, Figure 23). The blockage is predominantly to the Southwest and North. This is likely due to trees and farming equipment or buildings. As with the CSAPR2, no partial beam blockage corrections are applied for the b-level data.

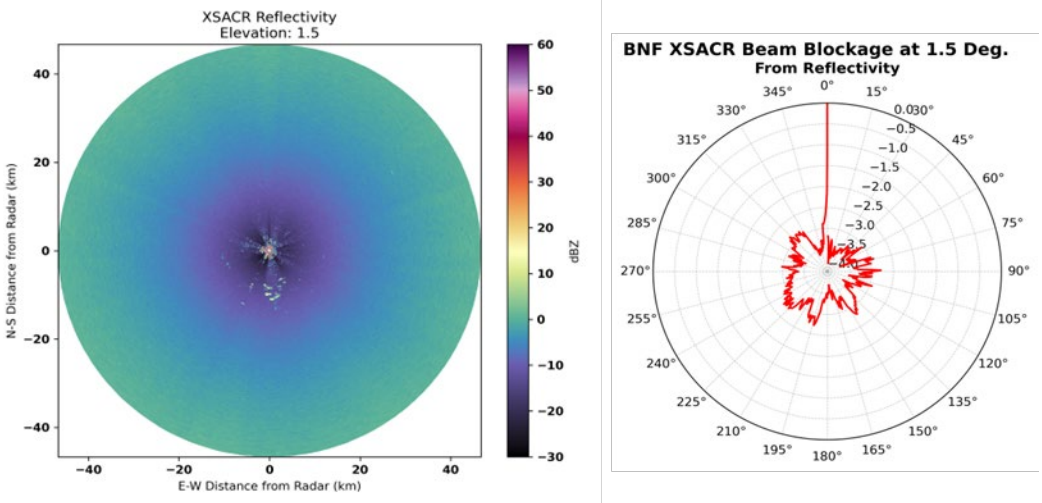

Figure 23. a) BNF XSACR PPI of reflectivity (dBZ) at 1.5 degrees elevation on a clear day and b) average reflectivity between 32.7 and 46.7 km across 10 clear days, highlighting the azimuth angles where beam blockage is maximized.

4.5.2 PLO Fluctuations

The XSACR phase-locked oscillator (PLO) experienced intermittent faults starting on May 31, 2025, which caused stripes to appear in the data and changes to background noise (Figure 24). While cloud data do not appear to be affected by this, please use caution when using data during times when the PLO is faulting and the sky noise is high.

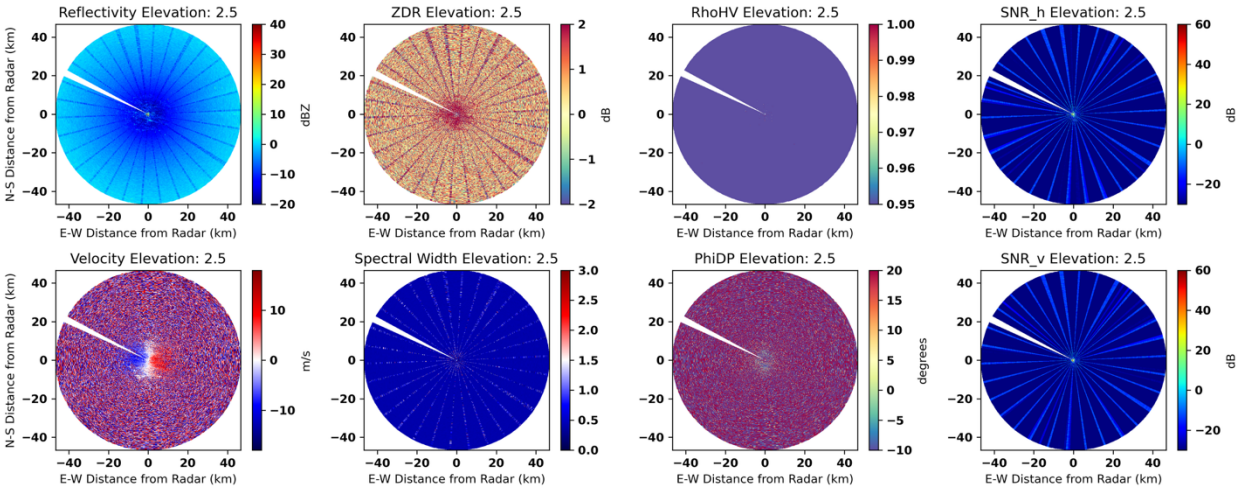

Figure 24. BNF XSACR case example during a time when the PLO was faulting. The striping is present in reflectivity, ZDR, spectral width, and signal-to-noise ratio.

4.5.3 Sweep Cutting

The SACR has an issue with sweep cutting, where the first sweep of a file is sometimes missed (Figure 25). The data for the first sweep are still present in the file, but the sweep start and end may need to be added manually. A fix is being developed but is not yet available.

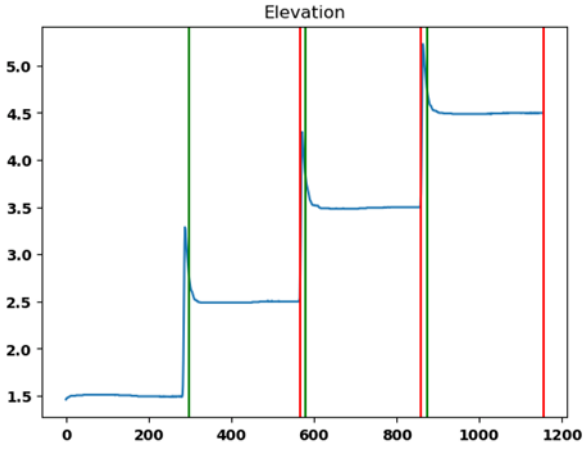

Figure 25. An example of the BNF SACR sweep-cutting issue, affecting both the X and KA data. Green vertical lines are sweep starts recorded in the file, while the red are sweep ends from the file.

5.0 KaSACR

5.1 Reflectivity Offsets

The mean daily clutter reflectivity for the KaSACR showed previously in Figure 26 that while there was some variability day to day, the radar was quite stable throughout the time period.

The KaSACR systematic reflectivity offset was evaluated through comparisons with the corrected XSACR reflectivity, as they share the same pedestal. Data are first selected to only use data +/- 1 degree from vertical. They are then matched in space and filtered for data where both radars have an SNR greater than 0 dB, XSACR has a ρ_{hv} greater than 0.985, and the range is low to minimize attenuation. The offset did vary case to case, but overall had a mean offset of 10.4 dB, as shown in Figure 23.

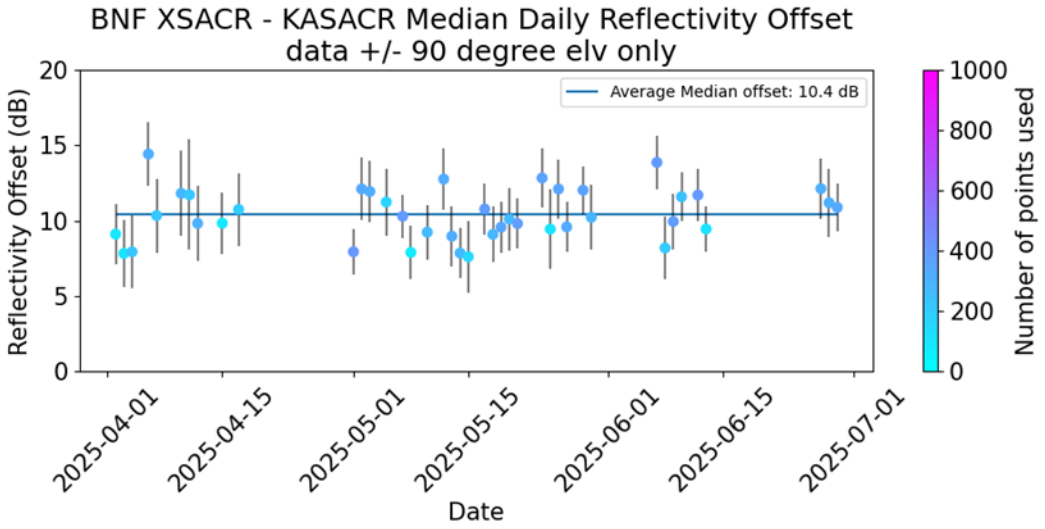

Figure 26. Time series of the daily median reflectivity differences between the XSACR and KaSACR. The color corresponds to the number of points passing thresholds, while the solid blue line shows the average median offset.

5.2 Censor Mask

The KaSACR, like the XSACR, does not include a built-in classification mask, so a simple censor mask is created to separate non-meteorological echoes, shown in Figure 27. The filters used for this mask are an SNR threshold of 0 dB.

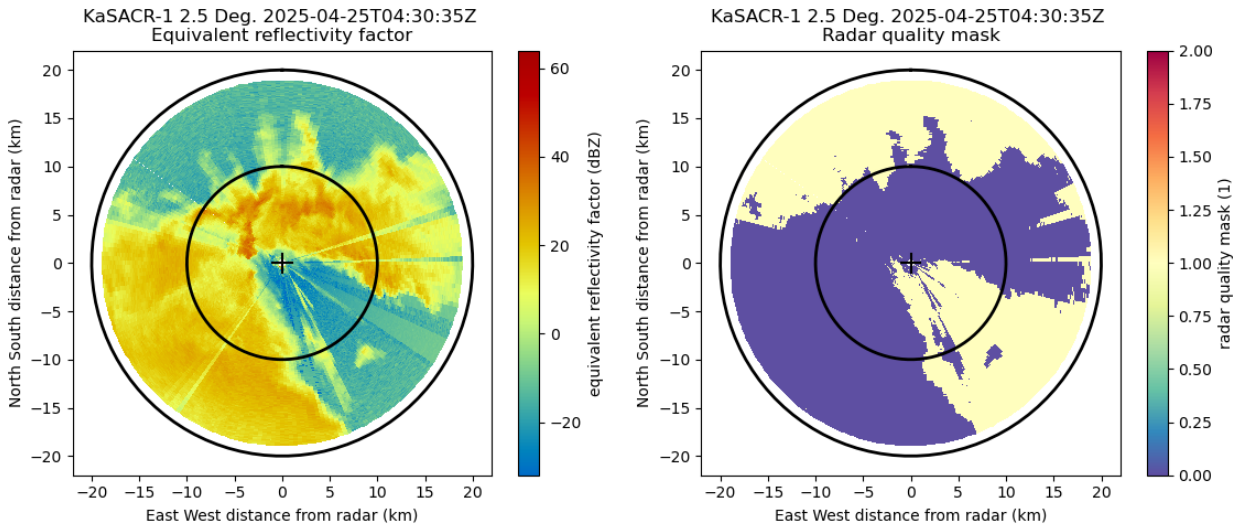

Figure 27. KaSACR PPI showing reflectivity (left) and censor mask (right) for a case on 25 April 2025.

5.3 Additional Data Quality Notes

5.3.1 Beam Blockage

The KaSACR experiences some beam blockage at the lowest elevation angle (1.5 degrees, Figure 23). The blockage is pretty uniform around the site, likely due to trees and farming equipment or buildings. As with the CSAPR2, no partial beam-blockage corrections are applied for the b-level data.

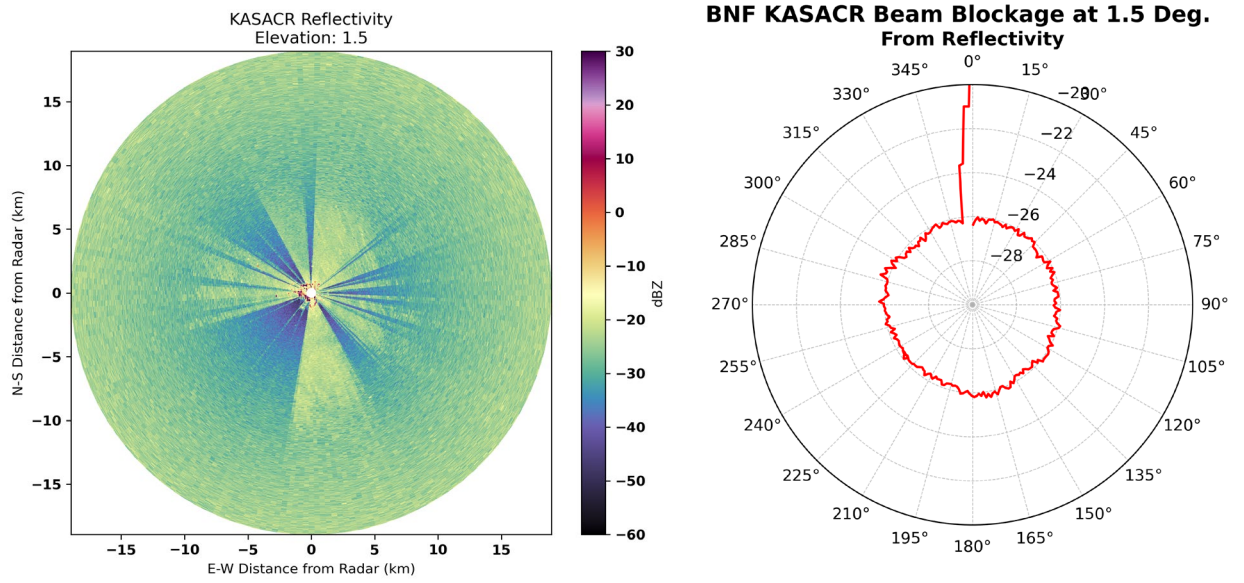

Figure 28. a) BNF KaSACR PPI of reflectivity (dBZ) at 1.5 degrees elevation on a clear day and b) average reflectivity between 10 and 18 km across 10 clear days, highlighting the azimuth angles where beam blockage is maximized.

6.0 Summary

A summary of the corrections applied for the BNF radars is shown in Table 4. The reflectivity date ranges for KAZR2 are 15 November-14 December 2024 (top) and 15 December 2024-30 June 2025 (bottom). Dates for the SACR and CSAPR2 offsets are from 1 April to 30 June 2025. In addition to the reflectivity corrections, the XSACR and CSAPR2 also have a ZDR correction, a KDP calculation, and (differential) attenuation estimates. New masks are also developed for the cloud radars to help identify cloudy regions.

Table 4. Summary of the b1 corrections applied to the BNF radars. The KAZR2 MD- and PR-mode reflectivity offsets for 15 December 2024 through 30 June 2025 are a function of time with an MD slope of 0.7 dB year^{-1} and a PR slope of 2.3 dB year^{-1}.

	KAZR2 GE	KAZR2 MD	KAZR2 PR	KaSACR	XSASCR	CSAPR2
Reflectivity (dBZ)	0.0 -4.0	-0.8 -3.8 + 0.7*year	-0.3 -2.7 + 2.3*year	+10.4	+5.5	+1.9
ZDR (dB)	-	-	-	-	+0.0	+0.8
KDP (° km^{-1})	-	-	-	-	Yes	Yes
attenuation (dB km^{-1})	gas attenuation in c-level				hydrometeor attenuation with KDP $A_h = 0.292 * KDP^{1.073}$ $A_{DP} = 0.046 * KDP^{1.105}$	hydrometeor attenuation with KDP $A_h = 0.0575 * KDP^{1.066}$ $A_{DP} = 0.0133 * KDP^{1.221}$
mask	censor_mask classification_mask			censor_mask	censor_mask	classification_mask

7.0 Description of Data Files

Some of the key variables in the b1-level datastreams for the BNF radars are listed below.

Key
New variable calculated in b1 data
Correction applied
New variable and correction applied

KAZR File Contents (bnfkazr2cfrgeqcM1.b1, bnfkazr2cfrmdqcM1.b1, and bnfkazr2cfrprqcM1.b1)	
Moments	
co_to_crosspol_correlation_coeff	copolar to cross-polar correlation coefficient (also known at rhoxh)
linear_depolarization_ratio	linear depolarization ratio, channel unspecified
mean_doppler_velocity	radial mean Doppler velocity, positive for motion away from the instrument
mean_doppler_velocity_crosspolar_v	Doppler velocity, cross-polar for vertical channel
reflectivity	equivalent reflectivity factor with offset applied
signal_to_noise_ratio_copolar_h	signal to noise ratio, horizontal channel
signal_to_noise_ratio_crosspolar_v	signal to noise ratio, cross-polar for vertical channel
spectral_width	spectral width
spectral_width_crosspolar_v	spectral width, cross-polar for vertical channel
Masks	
censor_mask	Bit mask 0: no mask 4: velocity_texture_above_threshold
classification_mask	Non-meteorological echo classification mask 0: hydrometeor 1: background noise 2: ground clutter 3: sidelobe 4: biota

KaSACR File Contents (bnfkasacrcfrqcS4.b1)	
Moments	
co_to_crosspol_correlation_coeff	copolar to cross-polar correlation coefficient (also known at rhoxh)
crosspolar_differential_phase	cross-polar propagation phase shift
linear_depolarization_ratio_v	linear depolarization ratio, vertical channel
mean_doppler_velocity	radial mean Doppler velocity, positive for motion away from the instrument
mean_doppler_velocity_crosspolar_v	Doppler velocity, cross-polar for vertical channel
reflectivity	equivalent reflectivity factor with offset applied
signal_to_noise_ratio_copolar_h	signal to noise ratio, horizontal channel
signal_to_noise_ratio_crosspolar_v	signal to noise ratio, vertical channel
spectral_width	spectral width
Masks	
censor_mask	Bit mask 0: no mask 1: SNR < 0

XSACR File Contents (bnfxsacrcfrqcS4.b1)	
Moments	
attenuation_corrected_differential_reflectivity	rainfall attenuation-corrected differential reflectivity (includes attenuation and offset)
attenuation_corrected_reflectivity_h	rainfall attenuation-corrected reflectivity, horizontal channel (includes attenuation and offset)
copol_correlation_coeff	copolar correlation coefficient (rhohv)
differential_phase	differential propagation phase shift
differential_reflectivity	differential reflectivity (ZDR) with offset applied
mean_doppler_velocity	radial mean Doppler velocity, positive for motion away from the instrument
reflectivity	equivalent reflectivity factor with offset applied
signal_to_noise_ratio_copolar_h	signal to noise ratio, horizontal channel
signal_to_noise_ratio_copolar_v	signal to noise ratio, vertical channel
specific_attenuation	specific attenuation at each bin; integral of this is applied for correction to attenuation_corrected_reflectivity_h
specific_differential_attenuation	specific differential attenuation at each bin; integral of this is applied for correction to attenuation_corrected_differential_reflectivity
specific_differential_phase	specific differential phase (KDP), calculated using reflectivity, differential phase, and range fields
spectral_width	spectral width
Masks	
censor_mask	Bit mask 0: no mask 1: SNR < 0 2: $\rho_{hv} < 0.985$

CSAPR2 File Contents (bnfcsapr2cfrqcS3.b1)	
Moments	
attenuation_corrected_differential_reflectivity	rainfall attenuation-corrected differential reflectivity (includes attenuation and offset)
attenuation_corrected_differential_reflectivity_lag_1	rainfall attenuation-corrected differential reflectivity at lag 1 (includes attenuation and offset)
attenuation_corrected_reflectivity_h	rainfall attenuation-corrected reflectivity, horizontal channel (includes attenuation and offset)
copol_correlation_coeff	copolar correlation coefficient (rhohv)
differential_phase	differential propagation phase shift
differential_reflectivity	differential reflectivity (ZDR) with offset applied
differential_reflectivity_lag_1	differential reflectivity at lag 1 with offset applied
mean_doppler_velocity	radial mean Doppler velocity, positive for motion away from the instrument
mean_doppler_velocity_v	radial mean Doppler velocity, vertical channel
normalized_coherent_power	normalized coherent power (NCP), also known as SQI
normalized_coherent_power_v	normalized coherent power, vertical channel
reflectivity	equivalent reflectivity factor with offset applied
reflectivity_v	equivalent reflectivity factor, vertical channel
signal_to_noise_ratio_copolar_h	signal to noise ratio, horizontal channel
signal_to_noise_ratio_copolar_v	signal to noise ratio, vertical channel
specific_attenuation	specific attenuation at each bin; integral of this is applied for correction to attenuation_corrected_reflectivity_h
specific_differential_attenuation	specific differential attenuation at each bin; integral of this is applied for correction to attenuation_corrected_differential_reflectivity
specific_differential_phase	specific differential phase (KDP), calculated using reflectivity, differential phase, and range fields
spectral_width	spectral width
spectral_width_v	spectral width, vertical channel
Masks	
censor_mask	censor mask, see variable details in the files for flags and meanings
classification_mask	classification mask 0: no mask 1: second trip 2: third trip 4: interference 8: clutter 16: sunspoke

8.0 References

Deng, M, SE Giangrande, MP Jensen, K Johnson, CR Williams, JM Comstock, Y-C Feng, A Matthews, IA Lindenmaier, TG Wendler, M Rocque, A Zhou, Z Zhu, E Luke, and D Wang. 2025. "Wet-radome attenuation in ARM cloud radars and its utilization in radar calibration using disdrometer measurements." *Atmospheric Measurement Techniques* 18(7): 1641–1657, https://doi.org/10.5194/amt-18-1641-2025

Feng, Y-C, A Matthews, M Rocque, M Deng, T Wendler, K Johnson, E Schuman, I Lindenmaier, V Castro, SE Giangrande, S Collis, R Jackson, A Theisen, and J Comstock. 2024. TRACER b1 Data Processing: Corrections, Calibrations, and Processing Report. U.S. Department of Energy, Atmospheric Radiation Measurement User Facility, Richland, Washington. DOE/SC-ARM-TR-297, https://doi.org/10.2172/2326212

Hardin, J, SE Giangrande, and A Zhou. 2020. Laser Disdrometer Quantities (LDQUANTS) and Video Disdrometer Quantities (VDISQUANTS) Value-Added Products Report. U.S. Department of Energy, Atmospheric Radiation Measurement User Facility, Richland, Washington. DOE/SC-ARM-TR-221, https://doi.org/10.2172/1808573

Hubbert, J, and VN Bringi. 1995. "An iterative filtering technique for the analysis of copolar differential phase and dual-frequency radar measurements." *Journal of Atmospheric and Oceanic Technology* 12(3): 643–648, https://doi.org/10.1175/1520-0426(1995)012<0643:AIFTFT>2.0.CO;2

Lang, T, B Dolan, N Guy, CA M Gerlach, J Hardin, and B Raut. 2024. CSU-Radarmet/CSU_RadarTools: CSU_RadarTools v1.4. Zenodo, https://doi.org/10.5281/zenodo.13975472

www.arm.gov

U.S. DEPARTMENT OF
ENERGY

Office of Science